Recipe for higher order topology on the triangular lattice

Philipp Eck,[1] Yuan Fang [⬤],[2] Domenico Di Sante [⬤],[3,4] Giorgio Sangiovanni [⬤],[1,*] and Jennifer Cano [⬤][2,4,†]

[1]*Institut für Theoretische Physik und Astrophysik and Würzburg-Dresden Cluster of Excellence ct.qmat,*
Universität Würzburg, 97074 Würzburg, Germany
[2]*Department of Physics and Astronomy, Stony Brook University, Stony Brook, New York 11794, USA*
[3]*Department of Physics and Astronomy, Alma Mater Studiorum, University of Bologna, 40127 Bologna, Italy*
[4]*Center for Computational Quantum Physics, Flatiron Institute, 162 5th Avenue, New York, New York 10010, USA*

We present a recipe for an electronic two-dimensional (2D) higher order topological insulator (HOTI) on a triangular lattice that can be realized in a large family of materials. The essential ingredient is mirror symmetry breaking, which allows for a finite quadrupole moment and trivial $\mathbb{Z}_2$ index. The competition between spin-orbit coupling and the symmetry-breaking terms gives rise to four topologically distinct phases; the HOTI phase appears when symmetry breaking dominates, including in the absence of spin-orbit coupling. We identify triangular monolayer adsorbate systems on the (111) surface of zincblende/diamond type substrates as ideal material platforms and predict the HOTI phase for $X = $ (Al, B, Ga) on SiC.

I. INTRODUCTION

A higher order topological insulator (HOTI) is a phase of matter that is gapped in its bulk and on its surfaces but exhibits gapless or midgap modes on its one-dimensional hinges or zero-dimensional corners, respectively, where two surfaces or edges meet [1–6]. Following the discovery of HOTIs, bismuth was immediately realized as a three-dimensional HOTI [6]. In two dimensions (2D), HOTIs were originally predicted in cold atoms [1] and have been realized in metamaterials [7–13]. However, an experimental demonstration of a 2D HOTI in an electronic system is still lacking.

In this paper, we present a tunable recipe for an electronic 2D HOTI that can be realized in a large class of hexagonal and trigonal material platforms. The theory is built on an angular momentum $l = 1$ (sub-)shell on the triangular lattice. The essential ingredient is symmetry breaking: Specifically, the absence of the horizontal reflection plane is necessary to open a hybridization gap, while the absence of the vertical reflection plane, in combination with the C_3 symmetry, allows for a well-defined and nonvanishing quadrupole moment [14–19]. Thus, mirror and inversion symmetry breaking is indispensable to realize the resulting HOTI phase: The phase is forbidden on the fully symmetric triangular lattice in this model. In addition, the HOTI does not require spin-orbit coupling (SOC): When the symmetry breaking is small, SOC opens a trivial gap, while it plays no role when the symmetry breaking dominates. These features are in contrast to the famous Kane-Mele model [20], where infinitesimal SOC opens a topological gap and inversion symmetry breaking ultimately trivializes the quantum spin Hall insulator (QSHI). In fact,

as we will show below, the HOTI phase cannot be achieved within the Kane-Mele model.

The main innovation of our work is to present a unified and realistic theory of HOTIs on the triangular lattice. Since 2D HOTIs are also obstructed atomic limits [1,2], we can classify them in terms of elementary band representations (EBRs). Our analysis of EBRs [21–24] gives insight into the physical mechanism behind corner charge driven by symmetry breaking. It includes earlier predictions of HOTIs in inversion-breaking transition-metal dichalcogenides [25–28] and is simpler than proposals requiring multiple atoms in the unit cell [29–35]. Identifying the essential ingredients allows us to make material predictions based on symmetry criteria, which we verify by first principles calculations; one example is aluminum deposited on SiC.

II. TOPOLOGICAL PHASES DRIVEN BY SYMMETRY BREAKING

We present a general model that describes p orbitals, or, more generally, an $l = 1$ angular momentum subshell, on the triangular lattice with tunable in-plane and out-of-plane mirror symmetry-breaking terms and spin-orbit coupling. By varying these parameters, the model realizes four phases, as depicted in Fig. 1. Figure 1 also reveals the surprising property that the symmetry-breaking terms are indispensable to realizing nontrivial topology: Specifically, when local SOC dominates over all symmetry-breaking terms, the ground state is topologically trivial, while in the limit of vanishing SOC, the HOTI phase is realized. When only one symmetry-breaking term dominates over spin-orbit coupling, the system is in a $\mathbb{Z}_2$ QSHI phase. The QSHI phase shown in Fig. 1(b) was recently realized in indenene, where symmetry breaking is provided by a SiC substrate [36–40].
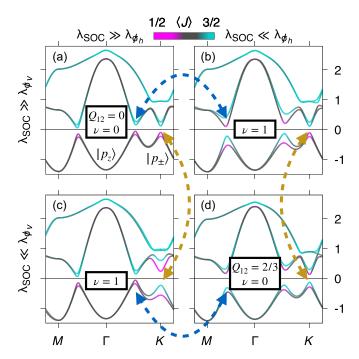
FIG. 1. Band structures indicating the $\mathbb{Z}_2$ topological invariant ν and quadrupole moment Q_{12} of the topologically distinct phases on the triangular lattice. The color code denotes the $\langle J \rangle$ character and the arrows indicate the relevant band inversion between neighboring phases. The labels in panel (a) denote the dominant orbital character of the valence bands.

The model is described by the Hamiltonian

$$\hat{H} = \hat{H}^T + \lambda_{\mathrm{SOC}}\hat{H}^{\mathrm{SOC}} + \lambda_{\phi_h}\hat{H}^{\phi_h} + \lambda_{\phi_v}\hat{H}^{\phi_v}, \qquad (1)$$

where each term is written explicitly in Appendix A. The first term, $\hat{H}^T$, describes the symmetry-allowed nearest neighbor hoppings in the inversion symmetric triangular lattice layer group (LG) p6/*mmm*, generated by a sixfold rotation, three vertical reflection planes σ_v, three diagonal reflection planes σ_d, and one horizontal reflection plane σ_h. The second term, $\hat{H}^{\mathrm{SOC}}$, is the local SOC interaction, which preserves the layer group symmetry and gaps the nodal line inside the BZ as well as the Dirac cones at the valley momenta; the gaps opened by SOC can be seen along $\Gamma - M$ and $\Gamma - K$ and at K/K'. Each of the two remaining terms breaks inversion symmetry in addition to a reflection symmetry. We use a strikeout notation to indicate the broken reflection symmetry. The third term, $\hat{H}^{\phi_h}$, breaks $z \mapsto -z$, which reduces the LG down to p6*mm*. It allows for hybridization between the states with magnetic quantum numbers $m = 0$ and $m = \pm 1$; i.e., it gaps the nodal line described above, which is formed when the $p_\pm$ bands cross the p_z bands. Finally, the last term, $\hat{H}^{\phi_v}$, breaks vertical reflection (σ_v) and (C_2) rotation. The sixfold rotation (C_6) reduces to C_3, resulting in the LG p$\bar{6}$m2 (if $\lambda_{\phi_h} = 0$). The absence of σ_v lowers the little group at the valley momenta from C_{3v} to C_3, splitting the two-dimensional representation describing p_+ and p_- orbitals into two one-dimensional chiral representations $(-m, +m)$ (for a more detailed discussion, see Appendix E). This term can be regarded as a nonlocal Semenoff mass term.

The competition between the inversion symmetry-breaking terms and the atomic SOC determines the topological phase of the model. The four insulating phases are separated from each other by gap-closing phase transitions that exchange bands, as indicated by the arrows in Fig. 1. Each gap reopening is accompanied by a band inversion that exchanges bands of predominately $J = 1/2$ character with those of $J = 3/2$ character, shown by the colors in Fig. 1. Simultaneously, the band inversion changes the $\mathbb{Z}_2$ invariant, ν, computed by tracking the Wilson loop eigenvalues [41,42]. The results can be summarized as follows: When SOC dominates [Fig. 1(a)], the valence (conduction) bands have the same value of $\langle J \rangle$ across the BZ. This indicates a $\nu = 0$ topologically trivial insulator, where the valence (conduction) bands transform as an atomic limit with $J = 1/2(J = 3/2)$. We dub this phase a "SOC insulator". By breaking either reflection symmetry, σ_h or σ_v, a $\nu = 1$ QSHI phase can be reached: in the former case, the hybridization between the p_z and the in-plane orbitals dominates over the SOC term along the nodal line, stabilizing an indenene-like QSHI phase [Fig. 1(b)] [39]. The other QSHI phase is characterized by a strong local orbital angular momentum polarization at the valley momenta, which gaps the in-plane Dirac bands ["ϕ_v QSHI," Fig. 1(c)]. Finally, if both symmetry-breaking terms dominate over SOC, or if SOC is absent, the $\mathbb{Z}_2$-index vanishes [Fig. 1(d)] again. However, the resulting insulator phase is not trivial: As we will show momentarily, it has a nontrivial polarization and filling anomaly, indicating that it is a HOTI and exhibits corner charge on a finite-sized lattice.

III. SYMMETRY INDICATORS AND POLARIZATION

The symmetry and topology of each phase is summarized in Table I. The strong topological invariants of the two $\nu = 1$ phases are not symmetry indicated due to the lack of inversion symmetry. However, the electric polarization and quadrupole moments of the HOTI and SOC insulating phases with $\nu = 0$ can be diagnosed by symmetry indicators [16–19] constructed from the EBRs [21,23,24].

To compute the symmetry indicators, we define lattice vectors $\mathbf{a}_1 = (1, 0)$, $\mathbf{a}_2 = (1/2, \sqrt{3}/2)$ and reciprocal lattice vectors $\mathbf{b}_1 = 2\pi(1, -1/\sqrt{3})$, $\mathbf{b}_2 = (0, 4\pi/\sqrt{3})$. The polarization vector with components in the directions of the two primitive lattice vectors is defined by $\mathbf{P} = (P_1, P_2) = -\langle(r_1, r_2)\rangle$, where $r_{1,2}$ are the relative coordinates of the point $\mathbf{r} = r_1\mathbf{a}_1 + r_2\mathbf{a}_2$. The quadrupole moment is given by $Q_{12} = -\langle r_1 r_2 + \frac{1}{4}(r_1^2 + r_2^2)\rangle$ in the presence of threefold rotation symmetry [16]. The symmetry indicators for polarization and quadrupole moment are [16–19]

$$P_1 = P_2 = -\tfrac{2}{3}([\#e^{i\pi/3}] - [\#e^{-i\pi/3}]) \mod 2, \qquad (2)$$

$$Q_{12} = -\tfrac{2}{3}([\#e^{i\pi/3}] + [\#e^{-i\pi/3}]) \mod 1, \qquad (3)$$

where $[\#\xi]$ is the number of valence bands with C_3 eigenvalue $\xi = e^{i\frac{2\pi}{3}j_z}$ at $\Gamma = \mathbf{0}$ subtracted from the number of valence bands with C_3 eigenvalue ξ at $K = \frac{2}{3}\mathbf{b}_1 + \frac{1}{3}\mathbf{b}_2$.

In all four phases, the valence bands at Γ are always p_z type with total magnetic quantum numbers $j_z = \{-1/2, +1/2\}$ [see Fig. 1(a)]. Consequently, only the rotation eigenvalues at K can change the electric polarization or quadrupole moment:

TABLE I. C_3 rotation eigenvalues and dipole/quadrupole moments of the insulating phases of Eq. (1). For each phase, the layer group indicated is the highest symmetry group that satisfies the inequalities in columns four and five. The electric multipoles in the $\nu = 1$ phases are ill defined. The little groups, irreps, and corresponding character tables of momenta Γ and K are shown in Appendix F.

Phase	Layer group	ν	SOC vs ϕ_h	SOC vs ϕ_v	$\xi(C_3)$ at K	$\mathbf{P} = (P_1, P_2)$	Q_{12}
SOC insulator	p6/mmm	0	$\lambda_{\mathrm{SOC}} \gg \lambda_{\phi_h}$	$\lambda_{\mathrm{SOC}} \gg \lambda_{\phi_v}$	$\{e^{+i\pi/3}, e^{-i\pi/3}\}$	$(0, 0)$ mod 2	0 mod 1
Indenene-like ϕ_h QSHI	p6mm	1	$\lambda_{\mathrm{SOC}} \ll \lambda_{\phi_h}$	$\lambda_{\mathrm{SOC}} \gg \lambda_{\phi_v}$	$\{e^{+i\pi/3}, e^{-i\pi/3}\}$	–	–
ϕ_v QSHI	p$\bar{6}$m2	1	$\lambda_{\mathrm{SOC}} \gg \lambda_{\phi_h}$	$\lambda_{\mathrm{SOC}} \ll \lambda_{\phi_v}$	$\{e^{\pm i\pi/3}, -1\}$	–	–
Triangular HOTI	p3m1	0	$\lambda_{\mathrm{SOC}} \ll \lambda_{\phi_h}$	$\lambda_{\mathrm{SOC}} \ll \lambda_{\phi_v}$	$\{e^{\pm i\pi/3}, -1\}$	$(\mp\frac{2}{3}, \mp\frac{2}{3})$ mod 2	$\frac{2}{3}$ mod 1

The competition between $\hat{H}^{\mathrm{SOC}}$ vs $\hat{H}^{\phi_v}$ acting on the $p_{\pm}$ subspace results in predominantly $j_z = \{-1/2, +1/2\}$ character in the valence bands when $\hat{H}^{\mathrm{SOC}}$ dominates and $j_z = \{\pm 1/2, \pm 3/2\}$ character when $\hat{H}^{\phi_v}$ dominates, where $\pm$ is determined by sign(λ_{ϕ_v}). Applying Eqs. (2) and (3), we find the following dipole and quadrupole moments for the two $\nu = 0$ phases: The SOC insulator has $\mathbf{P} = 0$, $Q_{12} = 0$, while the triangular HOTI has $\mathbf{P} = \mp(2/3, 2/3)$ mod 2, $Q_{12} = 2/3$ mod 1. These results are shown in Table I. The nonzero quadrupole moment for the triangular HOTI phase implies the existence of corner localized states, which we study in the next section.

A 2D HOTI with a gapped bulk and edges, but midgap states localized at corners, is also an obstructed atomic limit. Thus, our results can be phrased in terms of EBRs [21,23,24]: The valence bands of the SOC insulator transform as an EBR induced from the irreducible representation (irrep) $\bar{E}_{1u}$ of the site-symmetry group at the $1a = (0, 0)$ position, while the HOTI with sign(λ_{ϕ_v}) = +1 transforms as an EBR induced from the irrep $\bar{E}_1$ of the site-symmetry group of the $1b = (1/3, 1/3)$ position. (The irrep notation follows Ref. [43]. The irreps corresponding to the valence bands in each phase are listed in Appendix F.)

This change in EBRs indicates the transition to an obstructed atomic limit as the Wannier center shifts from $1a$ to $1b$, corresponding to the electronic charge center detaching from the lattice sites in the HOTI phase to create the nonzero polarization and quadrupole moment. Similarly, for sign(λ_{ϕ_v}) = −1 the Wannier center shifts from $1a$ to $1c = (2/3, 2/3)$, creating a nonzero polarization of the opposite sign, and the quadrupole moment remains invariant. Breaking the vertical mirror planes σ_v is imperative to realize this phase: Since σ_v maps $1b = (1/3, 1/3)$ onto $1c = (2/3, 2/3)$, its presence forbids a Wannier center on $1b$ without a partner on $1c$ and vice versa (see Appendix E for a more detailed discussion).

Note that such a HOTI phase cannot exist in the Kane-Mele model: A $\nu = 0$ insulating ground state can only be reached by breaking inversion symmetry to gap the Dirac fermions [20]. In this phase, the Wannier functions are localized on one of the two atomic sublattices; consequently, the system lacks a finite dipole and quadrupole moment.

IV. HOTI EDGE AND CORNER CHARGE

The electric dipole moment in the HOTI phase has important consequences for finite-size geometries. As shown in Fig. 2(a), the triangular lattice has two canonical edge terminations: the zigzag and the flat edge. The bulk polarization

$\mathbf{P}$, arising from Wannier centers located at $1b$ (blue dots) in Fig. 2(a), is parallel to the zigzag edge and normal to the flat edge; the latter favors metallic edge states [26,44]. For the model, the edge states of the flat termination are nondegenerate and possess a linear band crossing at Γ, as shown in Fig. 2(b) (the touching is quadratic in the limit of vanishing SOC). In contrast, the zigzag geometry has degenerate insulating edge states, shown in Fig. 2(c).

To isolate the fractionally filled corner states living in the bulk and edge gaps, we consider triangular flakes with the insulating zigzag termination. In the HOTI phase at charge neutrality, we find six degenerate exponentially corner-localized states that are one-third occupied at an energy within the bulk and edge gaps, as shown in Fig. 3(a) and in agreement with the corner charge of $Q_{12} = 2/3$ computed in the previous section. That there are two electrons to occupy the six midgap states at charge neutrality is referred to as the "filling anomaly," $\eta = 3Q_{12} = 2$, where the factor of three corresponds to the three corners of the triangular flake [14,15,17]. While the energy and hence the filling of the corner states can be tuned via a C_3-symmetric corner potential, the filling anomaly remains a protected observable of the HOTI phase.
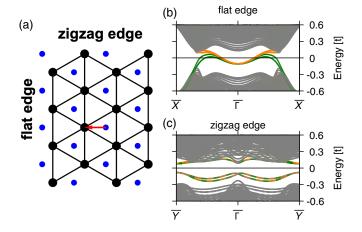

FIG. 2. Polarization and slab calculations for the HOTI phase with SOC. (a) The bulk dipole moment (red vector), resulting from Wannier centers located at the $1b$ Wyckoff position (blue dots) is perpendicular to the flat edge and parallel to the zigzag edge. [(b), (c)] Slab band structure and edge character (orange-green color code) for the two slab terminations. The polarization parallel (perpendicular) to the edge in the zigzag (flat) geometry yields insulating (metallic) edge states.
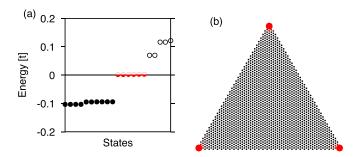
FIG. 3. Triangular flake spectrum and charge localization for the HOTI. At charge neutrality, there are exactly two electrons to fill the six midgap states shown in red in panel (a), in agreement with the filling anomaly $\eta = 2$. The point size in panel (b) shows the wave function localization of the red midgap states in panel (a).

For the flat-edge termination with finite edge polarization and metallic edge states [Fig. 2(a)], fractionally filled corner states can be only stabilized if the edge charge is compensated [16,17,26,27]. In a general finite-size flake, e.g., a round geometry, where all fundamental edge terminations are present, the corner states will be buried in the metallic edge continuum.

V. MATERIAL REALIZATION

Having established the existence of the HOTI phase in our minimal triangular model, we propose a general material realization concept: triangular adsorbate systems on the high symmetry sites of the (111) surface of zinc-blende/diamond-type substrates. This substrate provides three important ingredients: (1) structural stabilization of a triangular adsorbate monolayer; (2) symmetry breaking across the horizontal mirror plane to open a hybridization gap ($\hat{H}^{\phi_h}$); and (3) symmetry breaking across the vertical mirror planes ($\hat{H}^{\phi_v}$) to induce the bulk quadrupole moment.

We propose a monolayer of light group 3 elements (B, Al, Ga) on SiC and verify our prediction with an *ab initio* DFT study. For the T1 adsorption site of the Si-terminated surface, the adatom is located on top of the surface Si atom, while the C atom of the first SiC layer reduces the rotational symmetry of the triangular site from C_6 down to C_3 as shown in the inset of Fig. 4. In the case of Al, in-plane and out-of-plane reflection symmetry breaking (LG p3*m*1) dominates over SOC and results in an insulating bulk band structure with the p_z-type $\overline{\Gamma}_6(2)$ irrep and a $p_\pm$-type $\overline{K}_4(1) \oplus \overline{K}_6(1)$ irrep ($j_z = \{3/2, 1/2\}$) in the valence bands (see also Appendix F), identical to the triangular HOTI phase, as shown in Table I. Consequently, this phase has a quadrupole moment $Q_{12} = 2/3 \bmod 1$ and a corresponding corner charge.

Varying the group 3 elements, our *ab initio* calculations reveal a valley momenta gap of $\Delta_B = 0.49$ eV, $\Delta_{Al} = 0.24$ eV, and $\Delta_{Ga} = 0.22$ eV. As shown in Appendix D, only Al exhibits a direct band gap at the valley momenta; the global indirect band gap is 0.27 eV and 0.18 eV for B and Ga, respectively.

We verify the symmetry indicated prediction of corner charge by a first principles calculation on a finite size lattice for Al on SiC as summarized in Fig. 4. The insulating
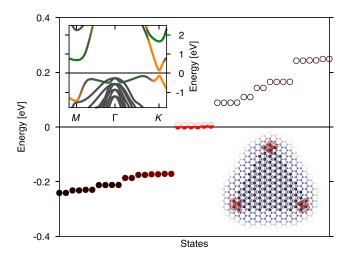

FIG. 4. The energy spectrum of a finite-size triangular flake of Al on SiC, truncated as shown in the lower inset. The red color code denotes the corner character of the state: The six degenerate midgap states are completely localized on the corners. Upper inset: bulk band structure of Al on SiC; color code denotes the Al p_z (green) and Al $p_\pm$ (orange) character. Lower inset: unit cell geometry and charge density of corner states: The C_6 symmetry of the Al (black) site on top of the Si atom (gray) is reduced to C_3 by the first C layer (blue).

band structure of its zigzag termination can be found in Appendix C. Indeed, although the in-gap position of the corner states is not crystal symmetry protected, the *ab initio* calculation reveals six degenerate states in the bulk band gap, which are filled with two electrons at charge neutrality. The charge density of these states are shown in the lower inset to Fig. 4, which are tightly localized to the corners. Furthermore, they display an almost perfect symmetry with respect to two of the three vertical mirror reflection planes of the bulk, even though these symmetries are broken at the edges and corners of the flake.

VI. CONCLUSION

We have proposed a recipe for electronic HOTIs in materials where the low-energy bands are composed of an $l = 1$ angular momentum subshell on a C_3-symmetric lattice. The essential ingredient is inversion- and reflection-symmetry breaking: On the symmetric triangular lattice, the HOTI phase is forbidden. We identified the HOTI phase using symmetry indicators and by an explicit calculation of the spectrum on a finite-sized triangular sample.

Our approach is very general and may be realized in many compounds by depositing adatoms onto the three-fold symmetric (111) surface of a zinc-blende/diamond substrate. We identified by first-principles calculations the $\mathbb{Z}_2$-trivial analogs of the recently synthesized QSHI indenene [39,45], namely B, Ga, and Al on SiC, as potential candidates and showed explicitly for the case of Al a full finite-size study: It is bulk insulating and has gapped edges and localized corner charge on a finite-sized triangular flake. Given the abundance of zinc-blende/diamond substrates (Si, C, GaAs, and InSb, for example), and a variety of potential adsorbates, we expect

many other material combinations will also realize the HOTI phase.

The presence of HOTI corner states could be detected via scanning tunneling microscopy. A proposal for detecting their quantized corner charge via atomic force microscopy has been put forth in Ref. [46]. By offering a realistic platform, our work paves the way to an experimental demonstration of a 2D electronic HOTI and may also inspire new techniques for more direct experimental observation.

A systematic *ab initio* study of the material combinations to determine which are bulk insulators will also be essential to future work. Upon extension to atoms with d and f orbitals, we expect "heavy" HOTIs with sizable electron-electron interactions and SOC.

APPENDIX A: TIGHT-BINDING MODEL

Here we describe the tight binding Hamiltonian of a p shell in the $\{p_x, p_y, p_z\}$ basis on a triangular lattice with the Bravais vectors $\mathbf{a}_1 = (1, 0)$ and $\mathbf{a}_2 = (0.5, \sqrt{3}/2)$.

1. Triangular lattice hopping Hamiltonian

The transition matrix elements H_{ij}^T allowed by the symmetries of LG p6/mmm can be obtained by following the approach of Slater and Koster [47]. They are given for an

TABLE II. Tight-binding parameters of the model Hamiltonian H^T in units of t.

E_z	V^σ	V^π	$V^\pi_{p_z}$
−0.7	0.7	−0.15	−0.25

TABLE III. Tight-binding parameters of the SOC and the symmetry-breaking model Hamiltonian terms in units of t. For each phase, the layer group with highest symmetry is given.

LG	λ_{SOC}	λ_{ϕ_h}	λ_{ϕ_v}
p6/mmm	0.30	0.1/6	0.04/3
p6mm	0.30	0.1	0.04/3
p$\bar{6}$m2	0.30	0.1/6	0.08
p3m1	0.15	0.1	0.04

orbital p_j located in the home unit cell (**0**) to an orbital p_i at site **R**:

$$H_{ii}^T(\mathbf{R}) = \langle p_i(\mathbf{0})|\hat{H}^T|p_i(\mathbf{R})\rangle = n_i^2 V_i^\sigma + \left(1 - n_i^2\right)V_i^\pi, \quad \text{(A1)}$$

$$H_{ij}^T(\mathbf{R}) = \langle p_i(\mathbf{0})|\hat{H}^T|p_j(\mathbf{R})\rangle = n_i n_j \left(V_{i,j}^\sigma - V_{i,j}^\pi\right), \quad \text{(A2)}$$

with $i = x, y, z$ and $i \neq j$. The coefficients n_i incorporate the in-plane orientation $[n_x = \cos(\phi)\sin(\theta)$, $n_y = \sin(\phi)\sin(\theta)$ and $n_z = \cos(\theta)]$ with the azimuthal angle $\phi(\mathbf{R})$ and polar angle $\theta(\mathbf{R})$. The transfer integral values V^σ and V^π in the p_{xy} subspace, the p_z transfer integral $V_{p_z}^\pi$, and the on-site energy shift of the p_z orbital E_z are given in Table II. The strength of the SOC interaction and the symmetry-breaking terms of the relevant layer groups are listed in Table III. All tight-binding parameters have been chosen such that an insulating ground state in the corresponding phase is stabilized. The overall band character reflects qualitatively the low-energy band structure of the group 3 elements on SiC, with p_z and p_{xy} valence band characters at Γ and K, respectively.

2. Atomic SOC

We consider full p-shell atomic spin orbit coupling, which is given in the $\{p_x, p_y, p_z\}$-basis by

$$\hat{H}^{\mathrm{SOC}} = \hat{L} \otimes \hat{S} \quad \text{(A3)}$$

$$= \frac{1}{2}\begin{pmatrix} 0 & -i\sigma_z & i\sigma_y \\ i\sigma_z & 0 & -i\sigma_x \\ -i\sigma_y & i\sigma_x & 0 \end{pmatrix}. \quad \text{(A4)}$$
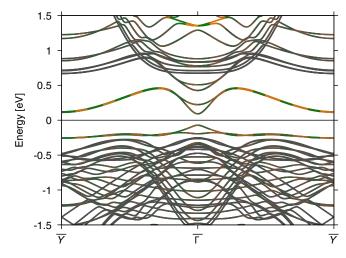

FIG. 5. Band structure for the zigzag ribbon geometry. The color code denotes the edge character, shown for alternating edges (dashed lines).
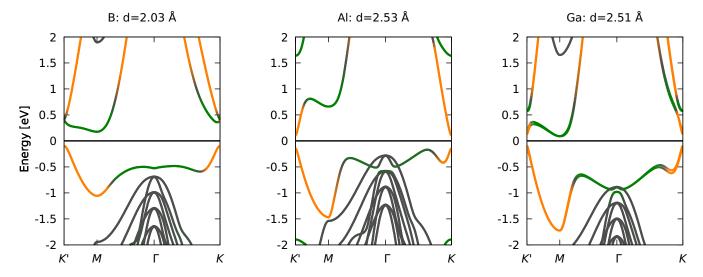
FIG. 6. Orbital resolved band character and equilibrium distances of the three adsorbate systems on four layers of SiC (0001). The color code denotes the $p_\pm$ (orange) and sp_z (green) orbital character.

Its matrix elements can be obtained by explicitly calculating the components of the orbital angular momentum and spin operators.

3. σ_h-symmetry breaking

The presence of vertical reflection symmetry prohibits the hybridization between the in-plane and out-of plane orbitals. When the symmetry is broken, the Slater-Koster integrals in Eqs. (A1) and (A2) become nonzero because the out-of-plane coordinates of the p_z and the in-plane orbitals differ, i.e., the polar angle $\theta \neq \pi/2$. The effective transfer elements read

$$H_{iz}^{\phi_h}(\mathbf{R}) = \langle p_i(\mathbf{0})|\hat{H}^{\phi_h}|p_z(\mathbf{R})\rangle = +n_i, \quad (A5)$$

$$H_{zi}^{\phi_h}(\mathbf{R}) = \langle p_z(\mathbf{0})|\hat{H}^{\phi_h}|p_i(\mathbf{R})\rangle = -n_i. \quad (A6)$$

4. σ_v-symmetry breaking

To break σ_v while preserving σ_d requires breaking C_{2z}. The absence of C_{2z} symmetry allows for the hopping terms to become asymmetric when the hopping direction is reversed. Since they must still respect the threefold rotation symmetry C_{3z}, such an interaction can be described by the following transfer matrix elements:

$$H_{yx}^{\phi_v}(\mathbf{R}) = \langle p_y(\mathbf{0})|\hat{H}^{\phi_v}|p_x(\mathbf{R})\rangle = +\cos(3\phi), \quad (A7)$$

$$H_{xy}^{\phi_v}(\mathbf{R}) = \langle p_x(\mathbf{0})|\hat{H}^{\phi_v}|p_y(\mathbf{R})\rangle = -\cos(3\phi), \quad (A8)$$

where $\phi(\mathbf{R})$ is the azimuthal angle. The opposite signs in Eqs. (A7) and (A8) are a consequence of the broken C_2 symmetry.

APPENDIX B: DFT METHODS

For our theoretical study of B, Al, and Ga on SiC(0001), we employed state-of-the-art first-principles calculations based on density functional theory as implemented in VASP [48] within the PAW method [49,50]. For the exchange-correlation potential, the PBE functional was used [51] by expanding the Kohn-Sham wave functions into plane waves up to energy cutoffs of 500 and 300 eV for the bulk calculations and for finite-size calculations, respectively. For the bulk calculations, we sampled the Brillouin zone on a $12 \times 12 \times 1$ regular mesh and SOC was self-consistently included [52]. We consider a (1×1) reconstruction of a triangular adatom monolayer adsorbed on the T1 position of Si-terminated SiC(0001) with an in-plane lattice constant of 3.07 Å. The equilibrium structure is obtained by relaxing all atoms until all forces converged below 0.001 eV/Å. For the bulk calculations, we consider four layers of SiC. To computationally access large lateral finite size systems, the substrate thickness is reduced to one layer of SiC. Electronic states arising from opposite surfaces are disentangled by a vacuum distance of at least 10 Å between periodic replicas in the z direction. The dangling bonds of the substrate terminated surface are saturated with hydrogen atoms.

TABLE IV. Irreps and dipole/quadrupole moments of the four insulating phases. For each phase, the layer group indicated is the highest symmetry group that satisfies the inequalities in columns four and five. The electric multipole moments in the $\nu = 1$ phases are ill defined.

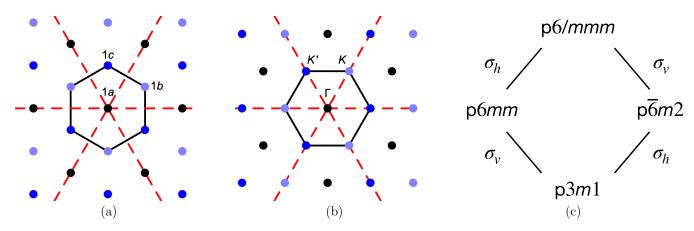| Phase	Layer group	ν	SOC vs ϕ_h	SOC vs ϕ_v	IRREPs Γ	IRREPs K	$\mathbf{P} = (P_1, P_2)$	Q_{12}
SOC insulator	p6/*mmm*	0	$\lambda_{SOC} \gg \lambda_{\phi_h}$	$\lambda_{SOC} \gg \lambda_{\phi_v}$	$\overline{\Gamma}_{12}(2)$	$\overline{K}_8(2)$	$(0, 0)$ mod 2	0 mod 1
Indenene-like ϕ_h QSHI	p6*mm*	1	$\lambda_{SOC} \ll \lambda_{\phi_h}$	$\lambda_{SOC} \gg \lambda_{\phi_v}$	$\overline{\Gamma}_9(2)$	$\overline{K}_6(2)$	–	–
ϕ_v QSHI	p$\overline{6}m2$	1	$\lambda_{SOC} \gg \lambda_{\phi_h}$	$\lambda_{SOC} \ll \lambda_{\phi_v}$	$\overline{\Gamma}_8(2)$	$\overline{K}_7(1) \oplus \overline{K}_{12}(1)$	–	–
Triangular HOTI	p3*m1*	0	$\lambda_{SOC} \ll \lambda_{\phi_h}$	$\lambda_{SOC} \ll \lambda_{\phi_v}$	$\overline{\Gamma}_6(2)$	$\overline{K}_4(1) \oplus \overline{K}_6(1)$	$(-\frac{2}{3}, -\frac{2}{3})$ mod 2	$\frac{2}{3}$ mod 1

FIG. 7. [(a), (b)] Impact of vertical reflection symmetry (red lines) on the hexagonal lattice. (a) The presence of σ_v maps the Wyckoff position $1b$ onto $1c$; thus, in groups with σ_v, the two Wyckoff positions merge into a single position with multiplicity two. (b) The rotation of real space and reciprocal space lattice by $\pi/6$ against each other translates σ_v into σ_d in momentum space (see also Table V). This introduces the vertical reflection to the little group of $1b$ and $1c$. (c) Real space layer group subgroup relation.

APPENDIX C: Al ON SiC EDGE STATES

Figure 5 shows the DFT band structure of a slab geometry with a zigzag edge termination. The width of 12 unit cells is chosen to be comparable to the height of the finite-size triangular flake. In agreement with the tight-binding model, the band structure is insulating and the edge states arising from opposite edges are energetically degenerate.

APPENDIX D: BULK BAND STRUCTURES OF B, Al, AND Ga ON SiC

The orbital character projected bulk band structures of B, Al, and Ga on SiC(0001) are shown in Fig. 6. All adsorbate systems show perfect qualitative agreement with the proposed HOTI model as they possess an insulating bulk band structure with massive in-plane Dirac cones at the valley momenta. The irreps of the valence bands are given in Table IV for LG p3m1 and indicate a nonvanishing bulk dipole and quadrupole moment. The weak SOC interaction in B and Al results in almost twofold degenerate bands, while the bands of the Ga monolayer possess a weak spin splitting.

APPENDIX E: VERTICAL REFLECTION SYMMETRY BREAKING IN REAL AND RECIPROCAL SPACE

We now describe the role of the vertical reflection symmetry in real and reciprocal space. As illustrated in Fig. 7,

if vertical reflections [red lines in Fig. 7(a)] are introduced, the LG p3m1 (or p$\bar{6}m2$) is promoted to p6mm (or p6/mmm) [the relationship between layer groups is shown in Fig. 7(c)]. The vertical reflection planes map the Wyckoff position $1b$ onto $1c$ (notation refers to LG p3m1), which results in a single Wyckoff position with a multiplicity of two in the more symmetric group. This explains why the bulk dipole moment, which requires an asymmetric charge distribution with respect to the $1b$ and $1c$ Wyckoff positions, is only allowed when σ_v is broken.

As the hexagonal real and reciprocal lattices are rotated relative to each other by $\pi/6$, the presence of σ_v in real space translates into σ_d in reciprocal space, as shown in Fig. 7(b). Thus, the reflection planes of σ_d leave the K and K' points invariant, which enlarges their little group from 3 to 3m. Since the group 3 only has one-dimensional single-valued irreps, in the absence of SOC, the σ_v-breaking term gaps the Dirac cones at K and K'. In the presence of SOC, it can still drive a band inversion at the valley momenta which is identified by the irreps. The little groups at each high symmetry point for each layer group are listed in Table V.

APPENDIX F: IRREDUCIBLE BAND REPRESENTATIONS

Table IV shows the irreps at high symmetry points for the four topological phases of our model. The labels of the irreps depend on the LG and can be derived from the characters tables shown in Tables VI, VII, VIII, X, IX, and XI. The notation follows Ref. [53]. All of the band structures (B, Al, and Ga on SiC) shown in Fig. 6 are classified by the irreps of the HOTI phase in LG p3m1.

TABLE V. Little groups at Γ and K for relevant layer groups.

Real space layer group	p6/mmm	p6mm	p$\bar{6}2m$	p3m1
Reciprocal space layer group	p6/mmm	p6mm	p$\bar{6}m2$	p31m
Little group at Γ	6/mmm	6mm	$\bar{6}2m$	3m
Little group at K	$\bar{6}m2$	3m	$\bar{6}$	3

TABLE VI. Character table for point group 6/*mmm*.

6/mmm	1	3_{001}	2_{001}	6_{001}	2_{100}	$2_{1\bar{1}0}$	d_1	$d_{3_{001}}$	$d_{6_{001}}$	-1	-3_{001}	m_{001}	-6_{001}	m_{100}	$m_{1\bar{1}0}$	d_{-1}	$d_{-3_{001}}$	$d_{-6_{001}}$
Γ_1^+	1	1	1	1	1	1	1	1	1	1	1	1	1	1	1	1	1	1
Γ_1^-	1	1	1	1	1	1	1	1	1	-1	-1	-1	-1	-1	-1	-1	-1	-1
Γ_2^+	1	1	1	1	-1	-1	1	1	1	1	1	1	1	-1	-1	1	1	1
Γ_2^-	1	1	1	1	-1	-1	1	1	1	-1	-1	-1	-1	1	1	-1	-1	-1
Γ_3^+	1	1	-1	-1	1	-1	1	1	-1	1	1	-1	-1	1	-1	1	1	-1
Γ_3^-	1	1	-1	-1	1	-1	1	1	-1	-1	-1	1	1	-1	1	-1	-1	1
Γ_4^+	1	1	-1	-1	-1	1	1	1	-1	1	1	-1	-1	-1	1	1	1	-1
Γ_4^-	1	1	-1	-1	-1	1	1	1	-1	-1	-1	1	1	1	-1	-1	-1	1
Γ_5^+	2	-1	2	-1	0	0	2	-1	-1	2	-1	2	-1	0	0	2	-1	-1
Γ_5^-	2	-1	2	-1	0	0	2	-1	-1	-2	1	-2	1	0	0	-2	1	1
Γ_6^+	2	-1	-2	1	0	0	2	-1	1	2	-1	-2	1	0	0	2	-1	1
Γ_6^-	2	-1	-2	1	0	0	2	-1	1	-2	1	2	-1	0	0	-2	1	-1
$\overline{\Gamma}_7$	2	-2	0	0	0	0	-2	2	0	2	-2	0	0	0	0	-2	2	0
$\overline{\Gamma}_8$	2	1	0	$-\sqrt{3}$	0	0	-2	-1	$\sqrt{3}$	2	1	0	$-\sqrt{3}$	0	0	-2	-1	$\sqrt{3}$
$\overline{\Gamma}_9$	2	1	0	$\sqrt{3}$	0	0	-2	-1	$-\sqrt{3}$	2	1	0	$\sqrt{3}$	0	0	-2	-1	$-\sqrt{3}$
$\overline{\Gamma}_{10}$	2	-2	0	0	0	0	-2	2	0	-2	2	0	0	0	0	2	-2	0
$\overline{\Gamma}_{11}$	2	1	0	$-\sqrt{3}$	0	0	-2	-1	$\sqrt{3}$	-2	-1	0	$\sqrt{3}$	0	0	2	1	$-\sqrt{3}$
$\overline{\Gamma}_{12}$	2	1	0	$\sqrt{3}$	0	0	-2	-1	$-\sqrt{3}$	-2	-1	0	$-\sqrt{3}$	0	0	2	1	$\sqrt{3}$

TABLE VII. Character table for point group $\bar{6}2m$.

$\bar{6}2m$	1	3_{001}	m_{001}	-6_{001}	2_{100}	$m_{1\bar{1}0}$	d_1	$d_{3_{001}}$	$d_{-6_{001}}$
Γ_1	1	1	1	1	1	1	1	1	1
Γ_2	1	1	-1	-1	1	-1	1	1	-1
Γ_3	1	1	-1	-1	-1	1	1	1	-1
Γ_4	1	1	1	1	-1	-1	1	1	1
Γ_5	2	-1	2	-1	0	0	2	-1	-1
Γ_6	2	-1	-2	1	0	0	2	-1	1
$\overline{\Gamma}_7$	2	-2	0	0	0	0	-2	2	0
$\overline{\Gamma}_8$	2	1	0	$-\sqrt{3}$	0	0	-2	-1	$\sqrt{3}$
$\overline{\Gamma}_9$	2	1	0	$\sqrt{3}$	0	0	-2	-1	$-\sqrt{3}$

TABLE VIII. Character table for point group 6*mm*.

6mm	1	3_{001}	2_{001}	6_{001}	m_{100}	$m_{1\bar{1}0}$	d_1	$d_{3_{001}}$	$d_{-6_{001}}$
Γ_1	1	1	1	1	1	1	1	1	1
Γ_2	1	1	1	1	-1	-1	1	1	1
Γ_3	1	1	-1	-1	-1	1	1	1	-1
Γ_4	1	1	-1	-1	1	-1	1	1	-1
Γ_5	2	-1	2	-1	0	0	2	-1	-1
Γ_6	2	-1	-2	1	0	0	2	-1	1
$\overline{\Gamma}_7$	2	-2	0	0	0	0	-2	2	0
$\overline{\Gamma}_8$	2	1	0	$-\sqrt{3}$	0	0	-2	-1	$\sqrt{3}$
$\overline{\Gamma}_9$	2	1	0	$\sqrt{3}$	0	0	-2	-1	$-\sqrt{3}$

TABLE IX. Character table for point group $\bar{6}$; $\epsilon = \frac{(1+i\sqrt{3})}{2}$.

$\bar{6}$	1	3_{001}^+	3_{001}^-	m_{001}	-6_{001}^-	-6_{001}^+	d_1	$d_{3_{001}^+}$	$d_{3_{001}^-}$	$d_{m_{001}}$	$d_{-6_{001}^-}$	$d_{-6_{001}^+}$
Γ_1	1	1	1	1	1	1	1	1	1	1	1	1
Γ_2	1	1	1	-1	-1	-1	1	1	1	-1	-1	-1
Γ_3	1	$-\bar{\epsilon}$	$-\epsilon$	1	$-\bar{\epsilon}$	$-\epsilon$	1	$-\bar{\epsilon}$	$-\epsilon$	1	$-\bar{\epsilon}$	$-\epsilon$
Γ_4	1	$-\bar{\epsilon}$	$-\epsilon$	-1	$\bar{\epsilon}$	ϵ	1	$-\bar{\epsilon}$	$-\epsilon$	-1	$\bar{\epsilon}$	ϵ
Γ_5	1	$-\epsilon$	$-\bar{\epsilon}$	1	$-\epsilon$	$-\bar{\epsilon}$	1	$-\epsilon$	$-\bar{\epsilon}$	1	$-\epsilon$	$-\bar{\epsilon}$
Γ_6	1	$-\epsilon$	$-\bar{\epsilon}$	-1	ϵ	$\bar{\epsilon}$	1	$-\epsilon$	$-\bar{\epsilon}$	-1	ϵ	$\bar{\epsilon}$
$\overline{\Gamma}_7$	1	-1	-1	$-i$	i	$-i$	-1	1	1	i	$-i$	i
$\overline{\Gamma}_8$	1	-1	-1	i	$-i$	i	-1	1	1	$-i$	i	$-i$
$\overline{\Gamma}_9$	1	$\bar{\epsilon}$	ϵ	$-i$	ϵ	$-\bar{\epsilon}$	-1	$-\bar{\epsilon}$	$-\epsilon$	i	$-\epsilon$	$\bar{\epsilon}$
$\overline{\Gamma}_{10}$	1	$\bar{\epsilon}$	ϵ	i	$-\epsilon$	$\bar{\epsilon}$	-1	$-\bar{\epsilon}$	$-\epsilon$	$-i$	ϵ	$-\bar{\epsilon}$
$\overline{\Gamma}_{11}$	1	ϵ	$\bar{\epsilon}$	$-i$	$\bar{\epsilon}$	$-\epsilon$	-1	$-\epsilon$	$-\bar{\epsilon}$	i	$-\bar{\epsilon}$	ϵ
$\overline{\Gamma}_{12}$	1	ϵ	$\bar{\epsilon}$	i	$-\bar{\epsilon}$	ϵ	-1	$-\epsilon$	$-\bar{\epsilon}$	$-i$	$\bar{\epsilon}$	$-\epsilon$

TABLE X. Character table for point group $3m$.

3m	1	3_{001}	$m_{1\bar{1}0}$	d_1	$d_{3_{001}}$	$d_{m_{1\bar{1}0}}$
Γ_1	1	1	1	1	1	1
Γ_2	1	1	-1	1	1	-1
Γ_3	2	-1	0	2	-1	0
$\bar{\Gamma}_4$	1	-1	$-i$	-1	1	i
$\bar{\Gamma}_5$	1	-1	i	-1	1	$-i$
$\bar{\Gamma}_6$	2	1	0	-2	-1	0

TABLE XI. Character table for point group 3; $\epsilon = \frac{(1+i\sqrt{3})}{2}$.

3	1	3_{001}^+	3_{001}^-	d_1	$d_{3_{001}^+}$	$d_{3_{001}^-}$
Γ_1	1	1	1	1	1	1
Γ_2	1	$-\bar{\epsilon}$	$-\epsilon$	1	$-\bar{\epsilon}$	$-\epsilon$
Γ_3	1	$-\epsilon$	$-\bar{\epsilon}$	1	$-\epsilon$	$-\bar{\epsilon}$
$\bar{\Gamma}_4$	1	-1	-1	-1	1	1
$\bar{\Gamma}_5$	1	$\bar{\epsilon}$	ϵ	-1	$-\bar{\epsilon}$	$-\epsilon$
$\bar{\Gamma}_6$	1	ϵ	$\bar{\epsilon}$	-1	$-\epsilon$	$-\bar{\epsilon}$

[1] W. A. Benalcazar, B. A. Bernevig, and T. L. Hughes, Quantized electric multipole insulators, Science **357**, 61 (2017).

[2] W. A. Benalcazar, B. A. Bernevig, and T. L. Hughes, Electric multipole moments, topological multipole moment pumping, and chiral hinge states in crystalline insulators, Phys. Rev. B **96**, 245115 (2017).

[3] J. Langbehn, Y. Peng, L. Trifunovic, F. von Oppen, and P. W. Brouwer, Reflection-Symmetric Second-Order Topological Insulators and Superconductors, Phys. Rev. Lett. **119**, 246401 (2017).

[4] Z. Song, Z. Fang, and C. Fang, $(d-2)$-Dimensional Edge States of Rotation Symmetry Protected Topological States, Phys. Rev. Lett. **119**, 246402 (2017).

[5] F. Schindler, A. M. Cook, M. G. Vergniory, Z. Wang, S. S. Parkin, B. A. Bernevig, and T. Neupert, Higher-order topological insulators, Sci. Adv. **4**, eaat0346 (2018).

[6] F. Schindler, Z. Wang, M. G. Vergniory, A. M. Cook, A. Murani, S. Sengupta, A. Y. Kasumov, R. Deblock, S. Jeon, I. Drozdov, H. Bouchiat, S. Guéron, A. Yazdani, B. A. Bernevig, and T. Neupert, Higher-order topology in bismuth, Nat. Phys. **14**, 918 (2018).

[7] M. Serra-Garcia, V. Peri, R. Süsstrunk, O. R. Bilal, T. Larsen, L. G. Villanueva, and S. D. Huber, Observation of a phononic quadrupole topological insulator, Nature (London) **555**, 342 (2018).

[8] C. W. Peterson, W. A. Benalcazar, T. L. Hughes, and G. Bahl, A quantized microwave quadrupole insulator with topologically protected corner states, Nature (London) **555**, 346 (2018).

[9] S. Imhof, C. Berger, F. Bayer, J. Brehm, L. W. Molenkamp, T. Kiessling, F. Schindler, C. H. Lee, M. Greiter, T. Neupert, and R. Thomale, Topolectrical-circuit realization of topological corner modes, Nat. Phys. **14**, 925 (2018).

[10] H. Xue, Y. Yang, F. Gao, Y. Chong, and B. Zhang, Acoustic higher-order topological insulator on a kagome lattice, Nat. Mater. **18**, 108 (2019).

[11] X. Ni, M. Weiner, A. Alu, and A. B. Khanikaev, Observation of higher-order topological acoustic states protected by generalized chiral symmetry, Nat. Mater. **18**, 113 (2019).

[12] J. Noh, W. A. Benalcazar, S. Huang, M. J. Collins, K. P. Chen, T. L. Hughes, and M. C. Rechtsman, Topological protection of photonic mid-gap defect modes, Nat. Photon. **12**, 408 (2018).

[13] H. Fan, B. Xia, L. Tong, S. Zheng, and D. Yu, Elastic Higher-Order Topological Insulator with Topologically Protected Corner States, Phys. Rev. Lett. **122**, 204301 (2019).

[14] W. A. Benalcazar, T. Li, and T. L. Hughes, Quantization of fractional corner charge in c_n-symmetric higher-order topological crystalline insulators, Phys. Rev. B **99**, 245151 (2019).

[15] F. Schindler, M. Brzezińska, W. A. Benalcazar, M. Iraola, A. Bouhon, S. S. Tsirkin, M. G. Vergniory, and T. Neupert, Fractional corner charges in spin-orbit coupled crystals, Phys. Rev. Res. **1**, 033074 (2019).

[16] H. Watanabe and S. Ono, Corner charge and bulk multipole moment in periodic systems, Phys. Rev. B **102**, 165120 (2020).

[17] Y. Fang and J. Cano, Filling anomaly for general two- and three-dimensional C_4 symmetric lattices, Phys. Rev. B **103**, 165109 (2021).

[18] Y. Fang and J. Cano, Classification of Dirac points with higher-order Fermi arcs, Phys. Rev. B **104**, 245101 (2021).

[19] R. Takahashi, T. Zhang, and S. Murakami, General corner charge formula in two-dimensional C_n-symmetric higher-order topological insulators, Phys. Rev. B **103**, 205123 (2021).

[20] C. L. Kane and E. J. Mele, Z_2 Topological Order and the Quantum Spin Hall Effect, Phys. Rev. Lett. **95**, 146802 (2005).

[21] B. Bradlyn, L. Elcoro, J. Cano, M. G. Vergniory, Z. Wang, C. Felser, M. I. Aroyo, and B. A. Bernevig, Topological quantum chemistry, Nature (London) **547**, 298 (2017).

[22] J. Kruthoff, J. de Boer, J. van Wezel, C. L. Kane, and R.-J. Slager, Topological Classification of Crystalline Insulators Through Band Structure Combinatorics, Phys. Rev. X **7**, 041069 (2017).

[23] H. C. Po, A. Vishwanath, and H. Watanabe, Symmetry-based indicators of band topology in the 230 space groups, Nat. Commun. **8**, 50 (2017).

[24] J. Cano, B. Bradlyn, Z. Wang, L. Elcoro, M. G. Vergniory, C. Felser, M. I. Aroyo, and B. A. Bernevig, Building blocks of topological quantum chemistry: Elementary band representations, Phys. Rev. B **97**, 035139 (2018).

[25] Z. Wang, B. J. Wieder, J. Li, B. Yan, and B. A. Bernevig, Higher-Order Topology, Monopole Nodal Lines, and the Origin of Large Fermi Arcs in Transition Metal Dichalcogenides $X\mathrm{Te}_2$ (X = Mo, W), Phys. Rev. Lett. **123**, 186401 (2019).

[26] J. Zeng, H. Liu, H. Jiang, Q.-F. Sun, and X. C. Xie, Multiorbital model reveals a second-order topological insulator in 1 h transition metal dichalcogenides, Phys. Rev. B **104**, L161108 (2021).

[27] S. Qian, G.-B. Liu, C.-C. Liu, and Y. Yao, C_n-symmetric higher-order topological crystalline insulators in atomically thin

transition metal dichalcogenides, Phys. Rev. B **105**, 045417 (2022).

[28] J. Sødequist, U. Petralanda, and T. Olsen, Abundance of second order topology in C_3 symmetric two-dimensional insulators, 2D Mater. **10**, 015009 (2023).

[29] M. Ezawa, Higher-Order Topological Insulators and Semimetals on the Breathing Kagome and Pyrochlore Lattices, Phys. Rev. Lett. **120**, 026801 (2018).

[30] B. Liu, G. Zhao, Z. Liu, and Z. Wang, Two-dimensional quadrupole topological insulator in γ-graphyne, Nano Lett. **19**, 6492 (2019).

[31] X.-L. Sheng, C. Chen, H. Liu, Z. Chen, Z.-M. Yu, Y. X. Zhao, and S. A. Yang, Two-Dimensional Second-Order Topological Insulator in Graphdiyne, Phys. Rev. Lett. **123**, 256402 (2019).

[32] M. J. Park, Y. Kim, G. Y. Cho, and S. B. Lee, Higher-Order Topological Insulator in Twisted Bilayer Graphene, Phys. Rev. Lett. **123**, 216803 (2019).

[33] E. Lee, R. Kim, J. Ahn, and B.-J. Yang, Two-dimensional higher-order topology in monolayer graphdiyne, npj Quantum Mater. **5**, 1 (2020).

[34] Y. Xue, H. Huan, B. Zhao, Y. Luo, Z. Zhang, and Z. Yang, Higher-order topological insulators in two-dimensional dirac materials, Phys. Rev. Res. **3**, L042044 (2021).

[35] M. Costa, G. R. Schleder, C. Mera Acosta, A. C. M. Padilha, F. Cerasoli, M. Buongiorno Nardelli, and A. Fazzio, Discovery of higher-order topological insulators using the spin Hall conductivity as a topology signature, npj Comput. Mater. **7**, 49 (2021).

[36] Z. F. Wang, K.-H. Jin, and F. Liu, Quantum spin Hall phase in 2d trigonal lattice, Nat. Commun. **7**, 12746 (2016).

[37] C. Si, K.-H. Jin, J. Zhou, Z. Sun, and F. Liu, Large-Gap Quantum Spin Hall State in Mxenes: d-Band Topological Order in a Triangular Lattice, Nano Lett. **16**, 6584 (2016).

[38] P. Chen, W. W. Pai, Y. H. Chan, W. L. Sun, C. Z. Xu, D. S. Lin, M. Y. Chou, A. V. Fedorov, and T. C. Chiang, Large quantum-spin-Hall gap in single-layer WSe$_2$, Nat. Commun. **9**, 2003 (2018).

[39] M. Bauernfeind, J. Erhardt, P. Eck, P. K. Thakur, J. Gabel, T.-L. Lee, J. Schäfer, S. Moser, D. Di Sante, R. Claessen, and G. Sangiovanni, Design and realization of topological Dirac fermions on a triangular lattice, Nat. Commun. **12**, 5396 (2021).

[40] P. Eck, C. Ortix, A. Consiglio, J. Erhardt, M. Bauernfeind, S. Moser, R. Claessen, D. Di Sante, and G. Sangiovanni,

Real-space obstruction in quantum spin Hall insulators, Phys. Rev. B **106**, 195143 (2022).

[41] A. A. Soluyanov and D. Vanderbilt, Computing topological invariants without inversion symmetry, Phys. Rev. B **83**, 235401 (2011).

[42] R. Yu, X. L. Qi, A. Bernevig, Z. Fang, and X. Dai, Equivalent expression of $\mathbb{z}_2$ topological invariant for band insulators using the non-Abelian Berry connection, Phys. Rev. B **84**, 075119 (2011).

[43] C. Bradley and A. Cracknell, *The Mathematical Theory of Symmetry in Solids: Representation Theory for Point Groups and Space Groups* (Oxford University Press, Oxford, UK, 2010).

[44] M. V. Bollinger, J. V. Lauritsen, K. W. Jacobsen, J. K. Nørskov, S. Helveg, and F. Besenbacher, One-Dimensional Metallic Edge States in MoS$_2$, Phys. Rev. Lett. **87**, 196803 (2001).

[45] J. Erhardt, M. Bauernfeind, P. Eck, M. Kamp, J. Gabel, T.-L. Lee, G. Sangiovanni, S. Moser, and R. Claessen, Indium epitaxy on SiC(0001): A roadmap to large scale growth of the quantum spin Hall insulator indenene, J. Phys. Chem. C **126**, 16289 (2022).

[46] H. Watanabe and H. C. Po, Fractional Corner Charge of Sodium Chloride, Phys. Rev. X **11**, 041064 (2021).

[47] J. C. Slater and G. F. Koster, Simplified LCAO method for the periodic potential problem, Phys. Rev. **94**, 1498 (1954).

[48] G. Kresse and J. Furthmüller, Efficient iterative schemes for *ab initio* total-energy calculations using a plane-wave basis set, Phys. Rev. B **54**, 11169 (1996).

[49] G. Kresse and D. Joubert, From ultrasoft pseudopotentials to the projector augmented-wave method, Phys. Rev. B **59**, 1758 (1999).

[50] P. E. Blöchl, Projector augmented-wave method, Phys. Rev. B **50**, 17953 (1994).

[51] J. P. Perdew, K. Burke, and M. Ernzerhof, Generalized Gradient Approximation Made Simple, Phys. Rev. Lett. **77**, 3865 (1996).

[52] S. Steiner, S. Khmelevskyi, M. Marsmann, and G. Kresse, Calculation of the magnetic anisotropy with projected-augmented-wave methodology and the case study of disordered Fe$_{1-x}$Co$_x$ alloys, Phys. Rev. B **93**, 224425 (2016).

[53] L. Elcoro, B. Bradlyn, Z. Wang, M. G. Vergniory, J. Cano, C. Felser, B. A. Bernevig, D. Orobengoa, G. Flor, and M. I. Aroyo, Double crystallographic groups and their representations on the Bilbao crystallographic server, J. Appl. Crystallogr. **50**, 1457 (2017).